SUPPORTING INFORMATION

Evolution of High Spin State Single-atom Catalyst Active Center in Na-O_2 Batteries

Jing Li[1‡], Aixiang Mao[1‡], Jia-hui Li[*], Honglai Liu[1,2], Cheng Lian[1,2*]

1. School of Chemistry and Molecular Engineering, East China University of Science and Technology, Shanghai 200237, P. R. China

2. State Key Laboratory of Chemical Engineering, School of Chemical Engineering, East China University of Science and Technology, Shanghai 200237, P. R. China

[*] Corresponding author: jiahuili@ecust.edu.cn, liancheng@ecust.edu.cn (C. L.)

[‡] These authors contributed equally to this work

Table of Contents

Figures

CoN_4 and corresponding spin-charge density. (e) The energy change during the activation of O_2. (f) The charge density difference of O_2@CoN_4.

Figure S10. (a) The schematic diagram of the configuration change of oxygen activation on NiN_3 and corresponding spin-charge density in initial state, state II, and final state. (b) The distance of Ni displacement and energy change during activation of O_2. (c) The charge density difference of O_2@NiN_3, where the yellow and cyan regions denote electron accumulation and depletion, respectively. The isosurface value is 0.0015 e $bohr^{-3}$. (d) The schematic diagram of the configuration change of oxygen activation on NiN_4 and corresponding spin-charge density. (e) The energy change during the activation of O_2. (f) The charge density difference of O_2@NiN_4.

Figure S11. The projected density of states (PDOS) of free O_2.

Figure S12. The projected density of states (PDOS) of O_2@MnN_3, O_2@CoN_3, O_2@NiN_3, O_2@MnN_4, O_2@CoN_4, and O_2@NiN_4, in which the red and blue shadows represent the d_{xy} orbital and d_z^2 orbital, respectively.

Figure S13. The optimized geometric structures of (a) NaO_2@MnN_3, (b) NaO_2@CoN_3, (c) NaO_2@NiN_3, (d) NaO_2@MnN_4, (e) NaO_2@CoN_4, and (f) NaO_2@NiN_4, respectively.

Figure S14. The optimized geometric structures of (a) Na_2O_2@MnN_3, (b) Na_2O_2@CoN_3, (c) Na_2O_2@NiN_3, (d) Na_2O_2@MnN_4, (e) Na_2O_2@CoN_4, and (f) Na_2O_2@NiN_4, respectively.

Figure S15. The optimized geometric structures of (a) Na_3O_2@MnN_3, (b) Na_3O_2@CoN_3, (c) Na_3O_2@NiN_3, (d) Na_3O_2@MnN_4, (e) Na_3O_2@CoN_4, and (f)

Na_3O_2@NiN_4, respectively.

Figure S16. The optimized geometric structures of (a) Na_4O_2@MnN_3, (b) Na_4O_2@CoN_3, (c) Na_4O_2@NiN_3, (d) Na_4O_2@MnN_4, (e) Na_4O_2@CoN_4, and (f) Na_4O_2@NiN_4, respectively.

Figure S17. The variations of relative energy against the time for AIMD simulations of (OMnO)N_3 at 1200 K.

Figure S18. The variations of relative energy against the time for AIMD simulations of (OCoO)N_3 at 1200 K.

Figure S19. The variations of relative energy against the time for AIMD simulations of (ONiO)N_3 at 1200 K.

Figure S20. The projected crystal orbital Hamilton population (pCOHP) of O_2 adsorbed on the MnN_3, CoN_3, NiN_3, MnN_4, CoN_4, and NiN_4, respectively.

Figure S21. The relative energy profiles of (a) the proximal path and (b) the distal path of the Na atom on CoN_3, (c) the proximal path and (d) the distal path of the Na atom on CoN_4.

Figure S22. The relative energy profiles of (a) the proximal path and (b) the distal path of the Na atom on NiN_3, (c) the proximal path and (d) the distal path of the Na atom on NiN_4.

Table S1. The adsorption modes of oxygen on SACs with two coordination types.

Table S2. The adsorption modes of metal atom or cluster on SACs with two coordination types.

Density functional theory (DFT) calculations

The geometry optimizations and energy calculations are approached by the Vienna *Ab initio* Simulation Package (VASP)[1]. The generalized gradient approximation (GGA) functional externalized by Perdew, Burke, and Ernzerhof (PBE)[2] is employed to describe the exchange-correlation energy within the Projector Augmented Wave (PAW) methods.[3] To ensure the calculation accuracy, a cutoff energy of 500 eV is adopted. The spin-polarized calculations are conducted until the self-consistent electronic energies and the ionic relaxation converged within 1×10^{-5} eV and 0.02 eV $Å^{-1}$, respectively. In all calculations, the van der Waals (vdW) interactions are estimated through the DFT-D3 method interpreted by Grimme[4]. The Brillouin zone is sampled using a Monkhorst-Pack 3×3×1 k-point grid. A 7×8 supercell carbon substrate is set. The threefold-coordinated catalyst model includes 108 carbon atoms, 3 nitrogen atoms, and 1 metal atom, while the four-coordinated catalyst model comprises 106 carbon atoms, 4 nitrogen atoms, and 1 metal atom. The GGA + U_{eff} method is applied to account for the strongly localized d orbitals of Mn, Co, and Ni in the selected structures. The Hubbard U_{eff} values for Mn, Co, and Ni are chosen to be 3.9[5], 5.3[6], and 5.3[7-8], respectively. The vacuum layer is set to be 25 Å for all the simulations to eliminate the interaction between adjacent molecular layers. The transition states of the O_2 activation and Na migration are implemented by the climbing image nudged elastic band (CI-NEB) method[9-10] at a reduced force criterion of 0.05 eV $Å^{-1}$. The obtained transition state is further verified by vibrational frequency calculation, and only one imaginary frequency is obtained for each transition state.

The formation energy of metal atoms with the MN_x is defined as:

$$E_f = E_{MN_x} - E_{NC} - E_M (M = Mn, Co, and Ni) * MERGEFORMAT (1)$$

where E_{MN_x} is the total energy of MN_x. E_{NC} is the energy of N-doped graphene with vacancies. E_M is the energy of the metal atom in the most stable bulk phase.

To evaluate the adsorption strength of Na, O_2, and the reaction intermediates Na_yO_2 (y = 1, 2, 3, and 4) on the substrate MN_x, their adsorption energies are calculated as

$$E_{ads}(Na) = E_{Na@sub} - E_{sub} - E_{Na} * MERGEFORMAT (2)$$

$$E_{ads}(O_2) = E_{O_2@sub} - E_{sub} - E_{O_2} * MERGEFORMAT (3)$$

$$E_{ads}(Na_yO_2) = E_{Na_yO_2@sub} - E_{sub} - E_{Na_yO_2} * MERGEFORMAT (4)$$

where $E_{Na@sub}$, $E_{O2@sub}$, and $E_{NayO2@sub}$ stand for the total energy of Na, O_2, and Na_yO_2 adsorbed on the MN_x, respectively. E_{sub} is the energy of the MN_x substrate. E_{Na}, E_{O2}, and E_{NayO2} denote the energy of the Na atom in the bulk phase structure, a free O_2 gas and Na_yO_2, respectively.

The reaction Gibbs free energy (ΔG) can be interpreted by

$$\Delta G = \Delta E + \Delta ZPE - T\Delta S + neU * MERGEFORMAT (5)$$

where ΔE is the electronic energy difference of the reaction. ΔZPE and ΔS denote the variations in zero-point energy and entropy, respectively. neU is the free energy contribution of the applied electrode potential.

The overpotential (η) is used to estimate the catalytic properties of doped SACs:

$$\eta_{ORR} = U_0 - U_{dc} * MERGEFORMAT (6)$$

$$\eta_{OER} = U_c - U_0 \qquad \text{* MERGEFORMAT (7)}$$

$$\eta_{TOT} = \eta_{ORR} + \eta_{OER} \qquad \text{* MERGEFORMAT (8)}$$

where U_0, U_{dc}, and U_c are the equilibrium, discharging, and charging potentials, respectively. U_{dc} is the maximum prerequisite voltage where all discharging steps are exothermic, while U_c refers to the minimum prerequisite voltage for all charging steps are exothermic. The total overpotential, η_{TOT}, is the sum of the overpotentials in ORR and OER processes.

The occupied d-band center of the metal atom was calculated by

$$\varepsilon_d = \frac{\int_{-\infty}^{E_F} \rho(E) E dE}{\int_{-\infty}^{E_F} \rho(E) dE} \qquad \text{* MERGEFORMAT (9)}$$

where $\rho(E)$ represents the projected density of states of the specified orbital. E_f is the Fermi energy.

Ab initio molecular dynamics (AIMD) simulation

AIMD simulations are conducted in canonical ensemble (NVT) at a temperature of 1200 K by using the Nosé–Hoover thermostat. The simulations employ a time step of 2 fs. A single gamma point is set to sample the Brillouin zone without considering the symmetry. The convergence criteria for energy and force are set to 10^{-4} eV and 0.02 eV $Å^{-1}$, respectively. 5000 steps are taken over a total time period of 10 ps at 1200 K referring to experimental synthesis temperature of SACs.

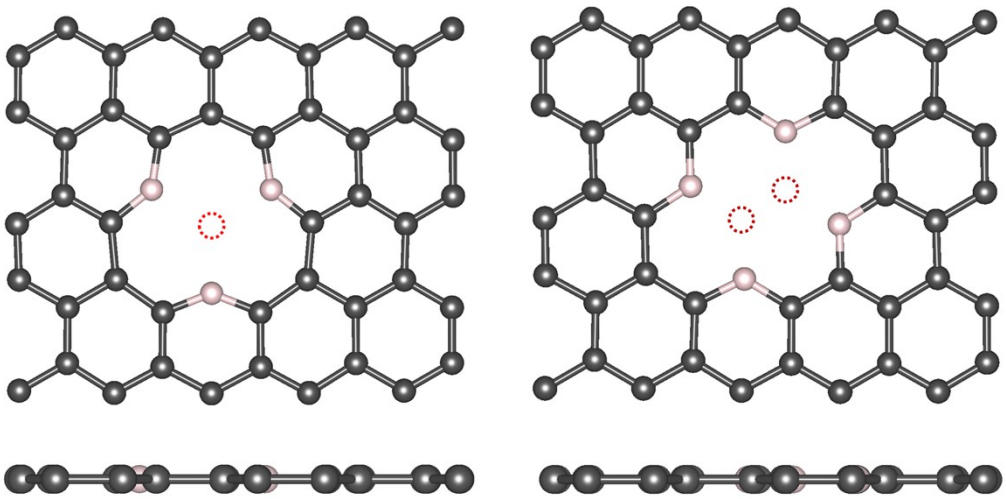

Figure S1. The schematic diagram of vacancy structure before metal substitution. The red dotted circles represent vacancy.

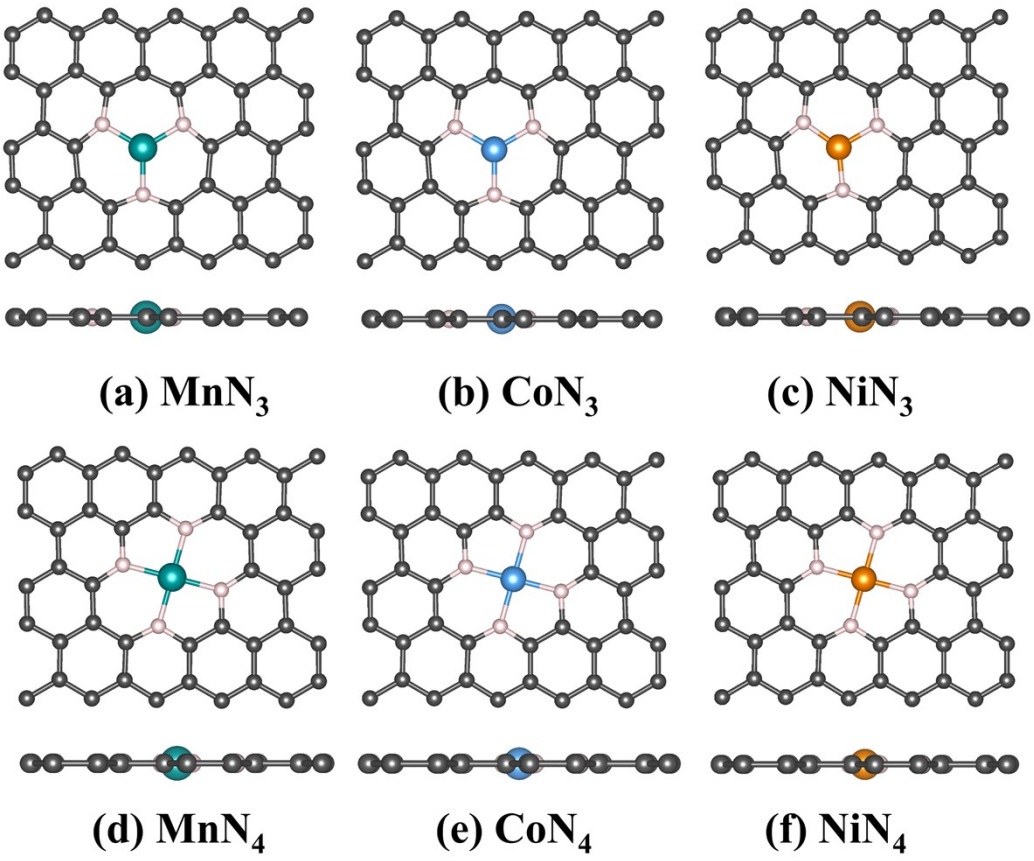

Figure S2. The optimized geometric structures of (a) MnN_3, (b) CoN_3, (c) NiN_3, (d) MnN_4, (e) CoN_4, and (f) NiN_4, respectively.

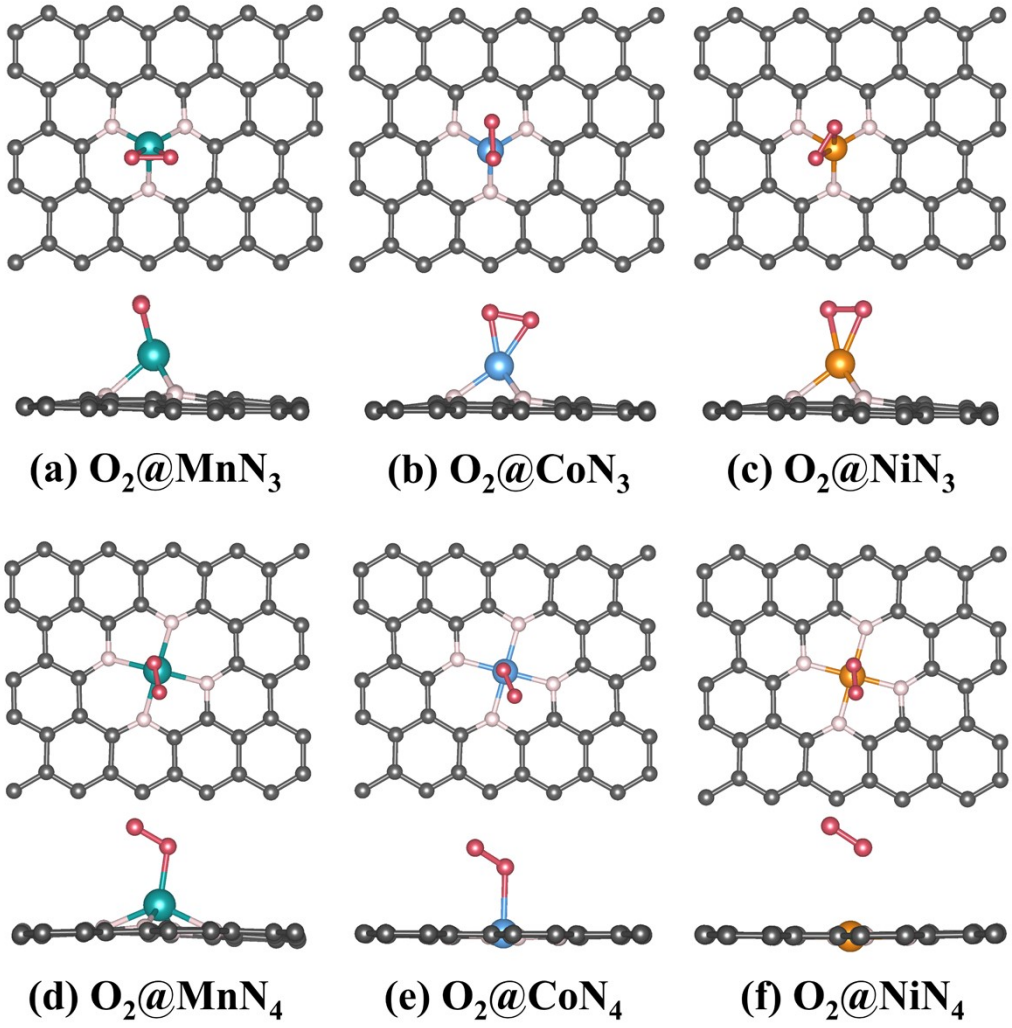

Figure S3. The optimized geometric structures of (a) O_2@MnN_3, (b) O_2@CoN_3, (c) O_2@NiN_3, (d) O_2@MnN_4, (e) O_2@CoN_4, and (f) O_2@NiN_4, respectively.

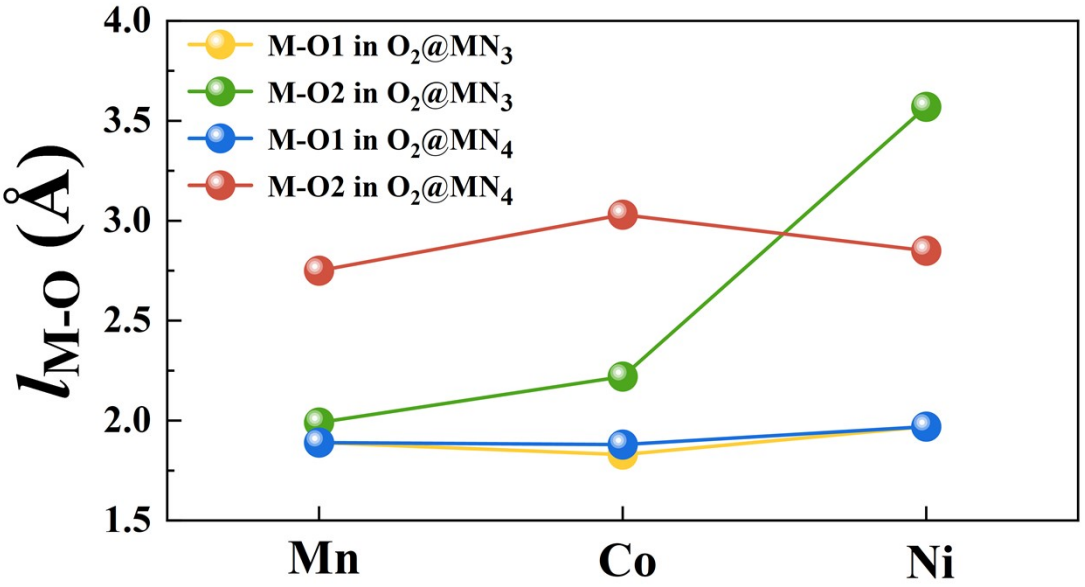

Figure S4. The M-O (M = Mn, Co, and Ni) bond length of O_2@MnN_3, O_2@CoN_3, O_2@NiN_3, O_2@MnN_4, O_2@CoN_4, and O_2@NiN_4.

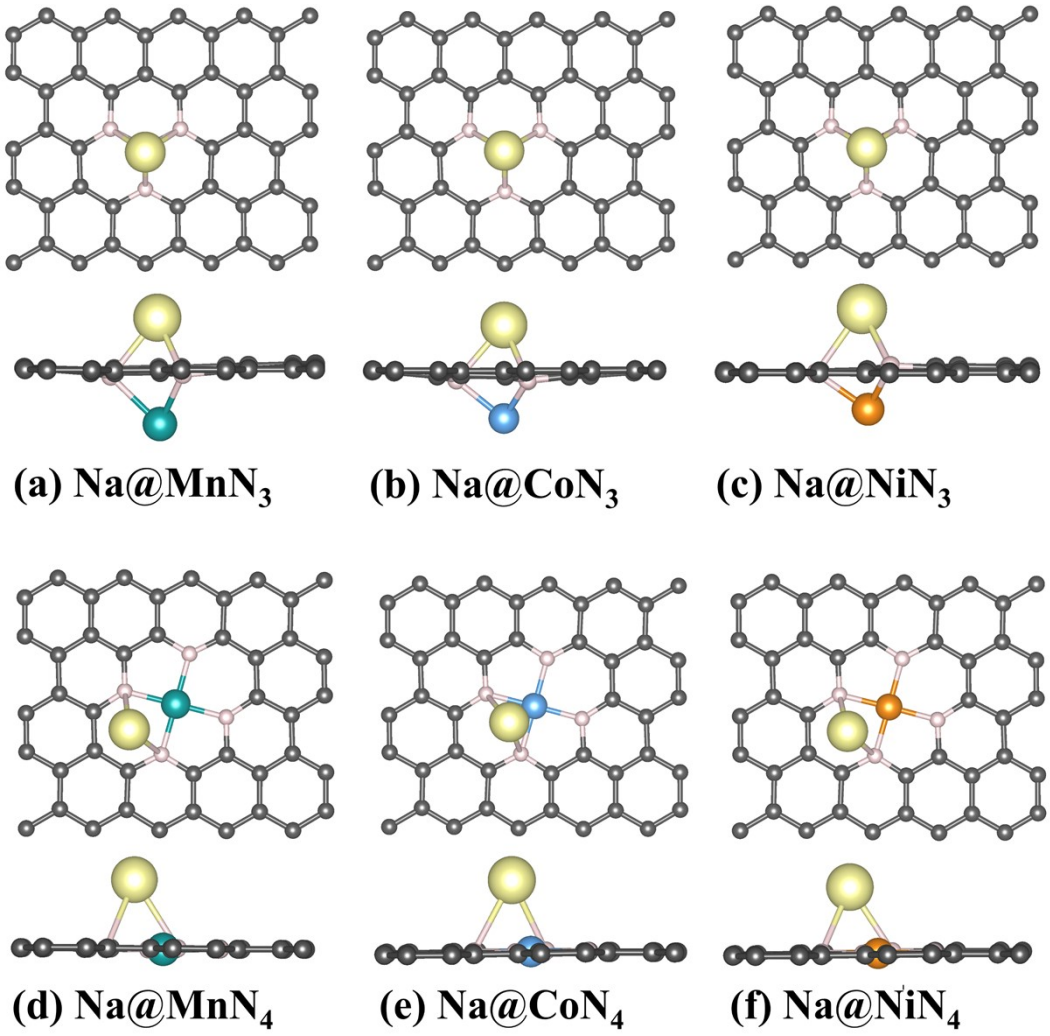

Figure S5. The optimized geometric structures of (a) $Na@MnN_3$, (b) $Na@CoN_3$, (c) $Na@NiN_3$, (d) $Na@MnN_4$, (e) $Na@CoN_4$, and (f) $Na@NiN_4$, respectively.

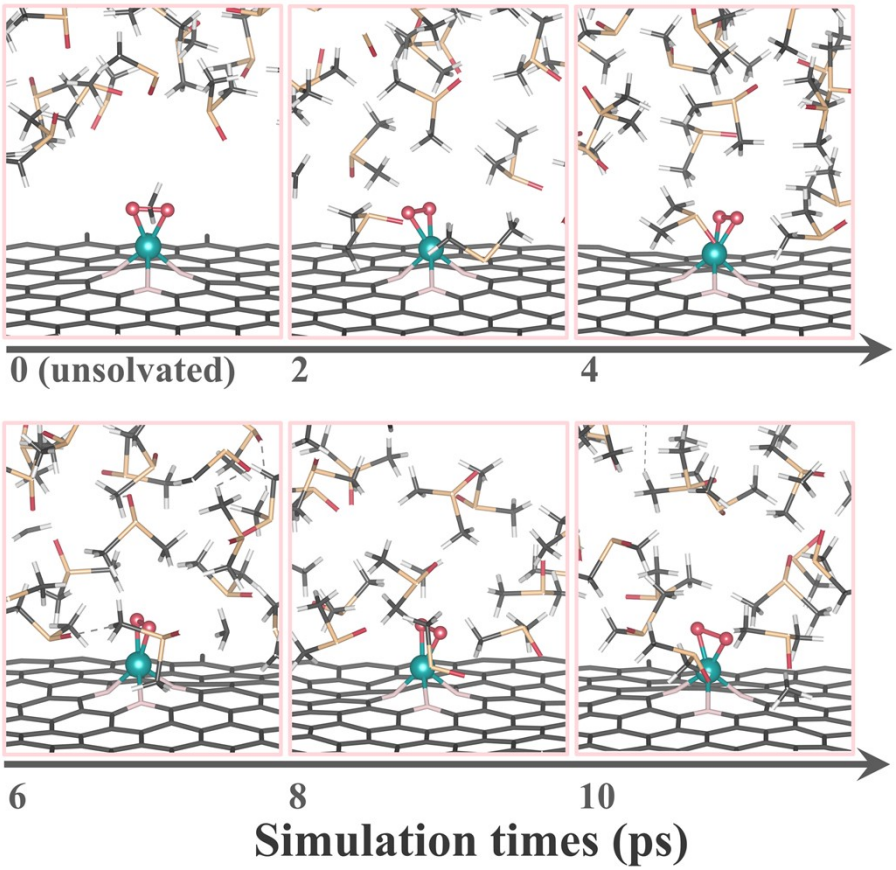

Figure S6. The selected snapshots of the AIMD trajectory for O_2 adsorption on MnN_3 in DMSO electrolyte.

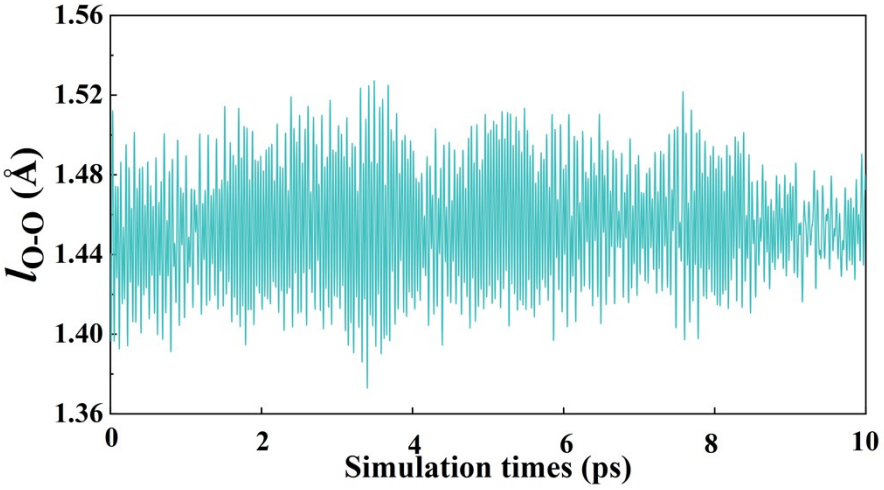

Figure S7. The O-O bond length of O_2@MnN_3 in AIMD simulation.

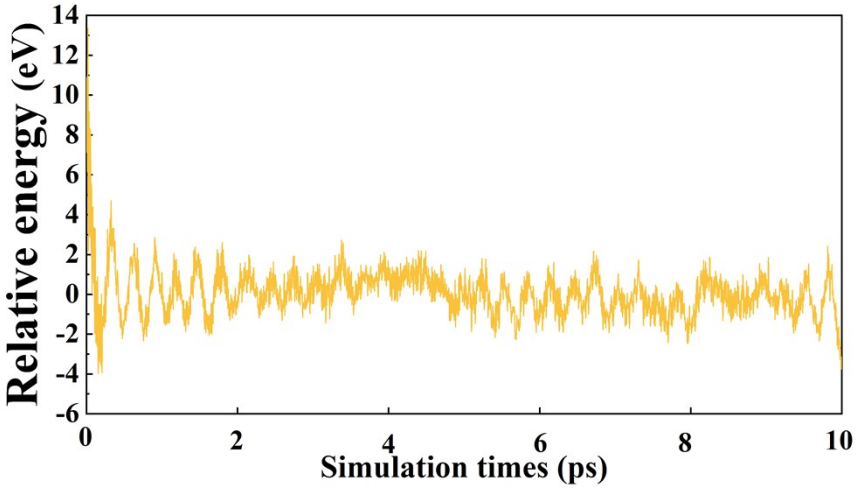

Figure S8. The relative energy of O_2@MnN_3 in AIMD simulation.

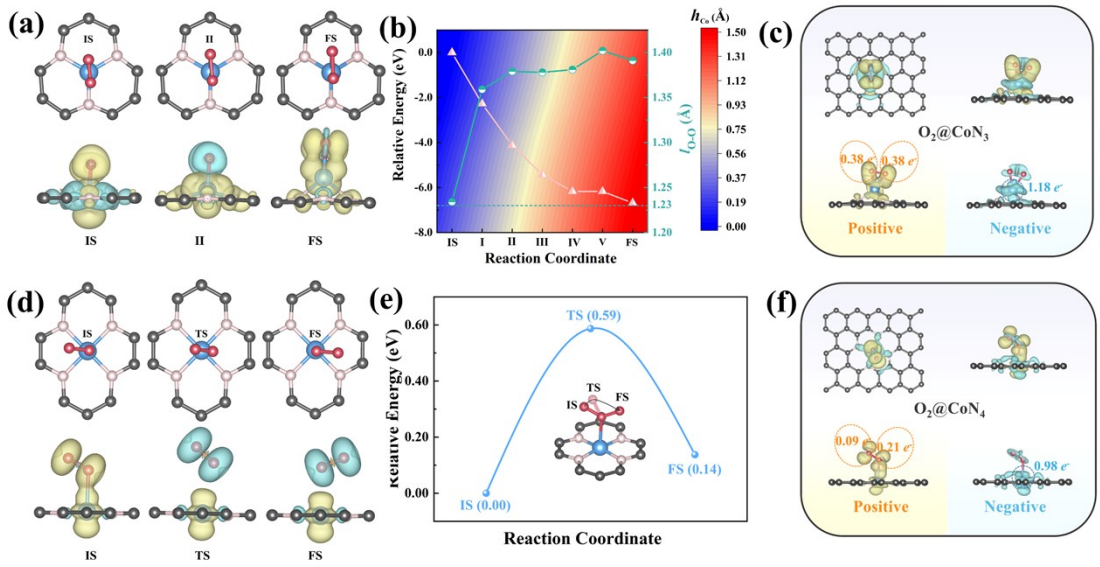

Figure S9. (a) The schematic diagram of the configuration change of oxygen activation on CoN_3 and corresponding spin-charge density in initial state, state II and final state. (b) The distance of Co displacement and energy change during activation of O_2. (c) The charge density difference of O_2@CoN_3, where the yellow and cyan regions denote electron accumulation and depletion, respectively. The isosurface value is 0.0015 e $bohr^{-3}$. (d) The schematic diagram of the configuration change of oxygen activation on CoN_4 and corresponding spin-charge density. (e) The energy change during the activation of O_2. (f) The charge density difference of O_2@CoN_4.

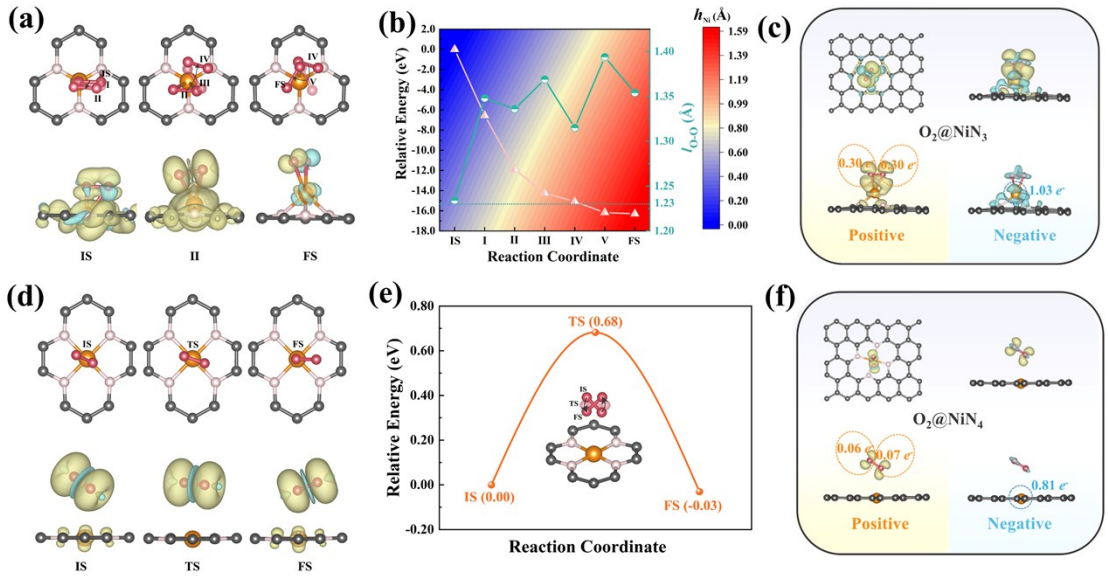

Figure S10. (a) The schematic diagram of the configuration change of oxygen activation on NiN_3 and corresponding spin-charge density in initial state, state II, and final state. (b) The distance of Ni displacement and energy change during activation of O_2. (c) The charge density difference of O_2@NiN_3, where the yellow and cyan regions denote electron accumulation and depletion, respectively. The isosurface value is 0.0015 e $bohr^{-3}$. (d) The schematic diagram of the configuration change of oxygen activation on NiN_4 and corresponding spin-charge density. (e) The energy change during the activation of O_2. (f) The charge density difference of O_2@NiN_4.

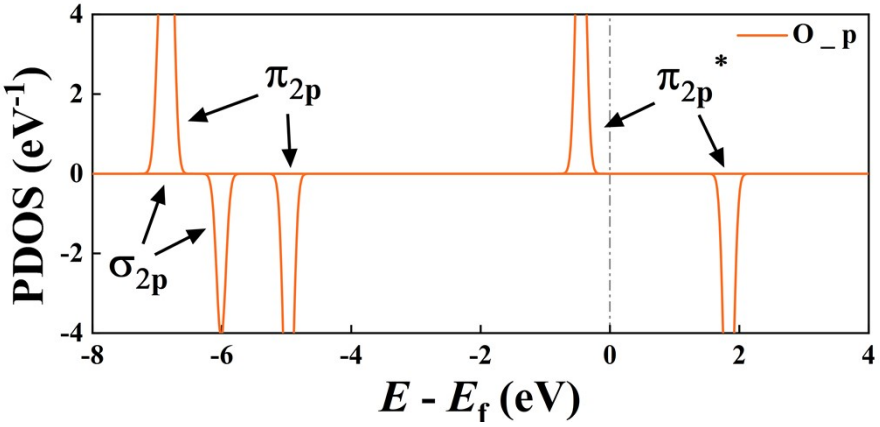

Figure S11. The projected density of states (PDOS) of free O_2.

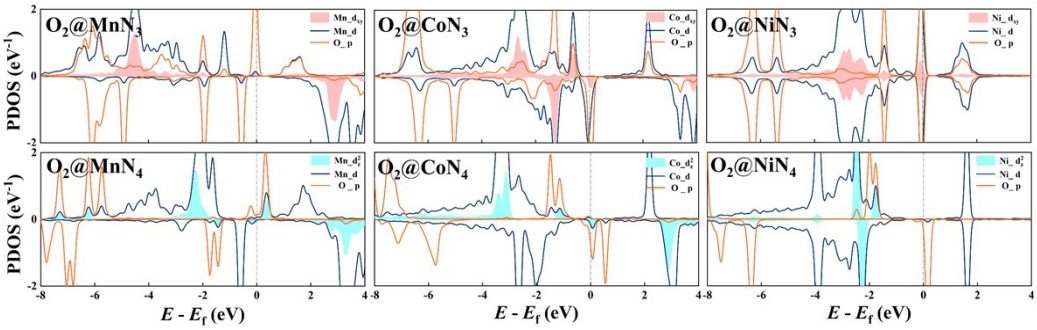

Figure S12. The projected density of states (PDOS) of O_2@MnN_3, O_2@CoN_3, O_2@NiN_3, O_2@MnN_4, O_2@CoN_4, and O_2@NiN_4, in which the red and blue shadows represent the d_{xy} orbital and d_z^2 orbital, respectively.

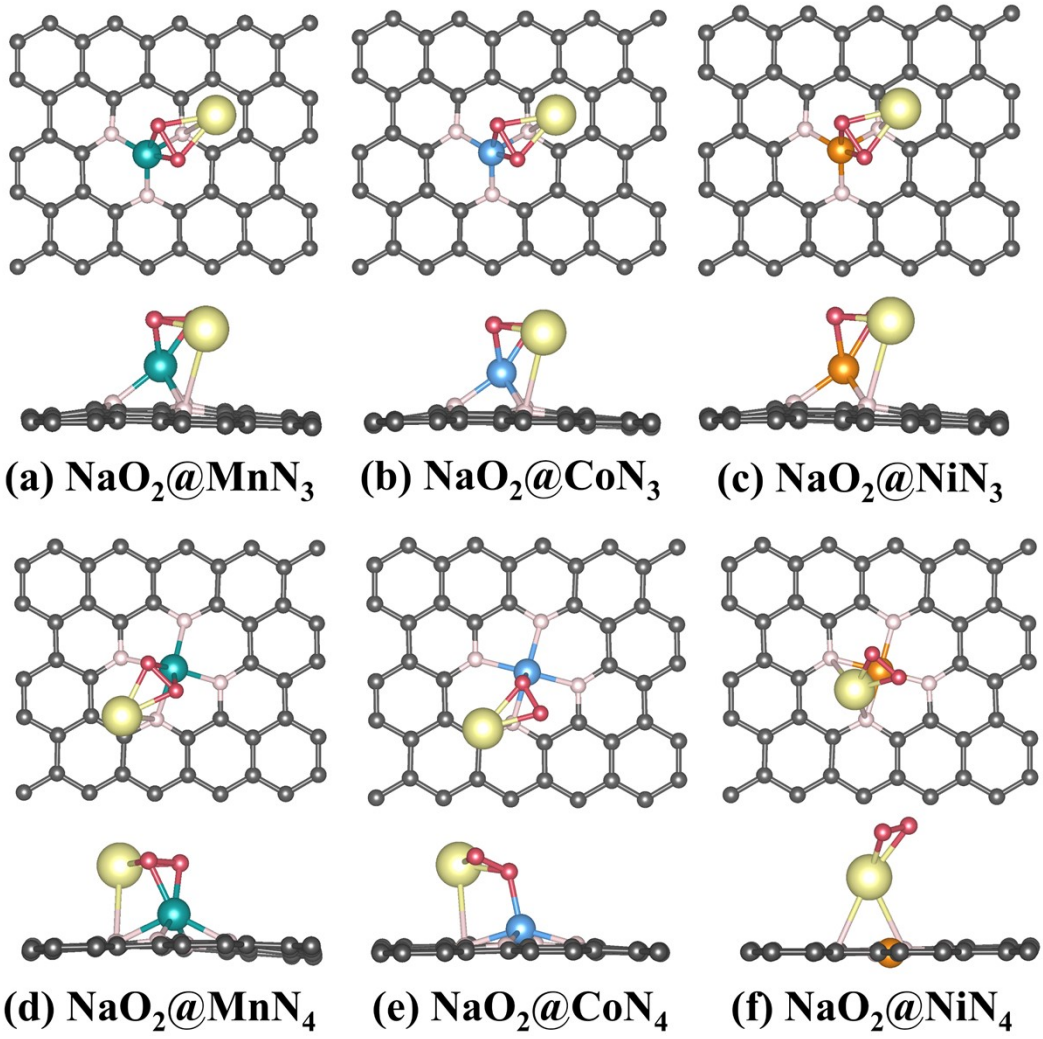

Figure S13. The optimized geometric structures of (a) $NaO_2@MnN_3$, (b) $NaO_2@CoN_3$, (c) $NaO_2@NiN_3$, (d) $NaO_2@MnN_4$, (e) $NaO_2@CoN_4$, and (f) $NaO_2@NiN_4$, respectively.

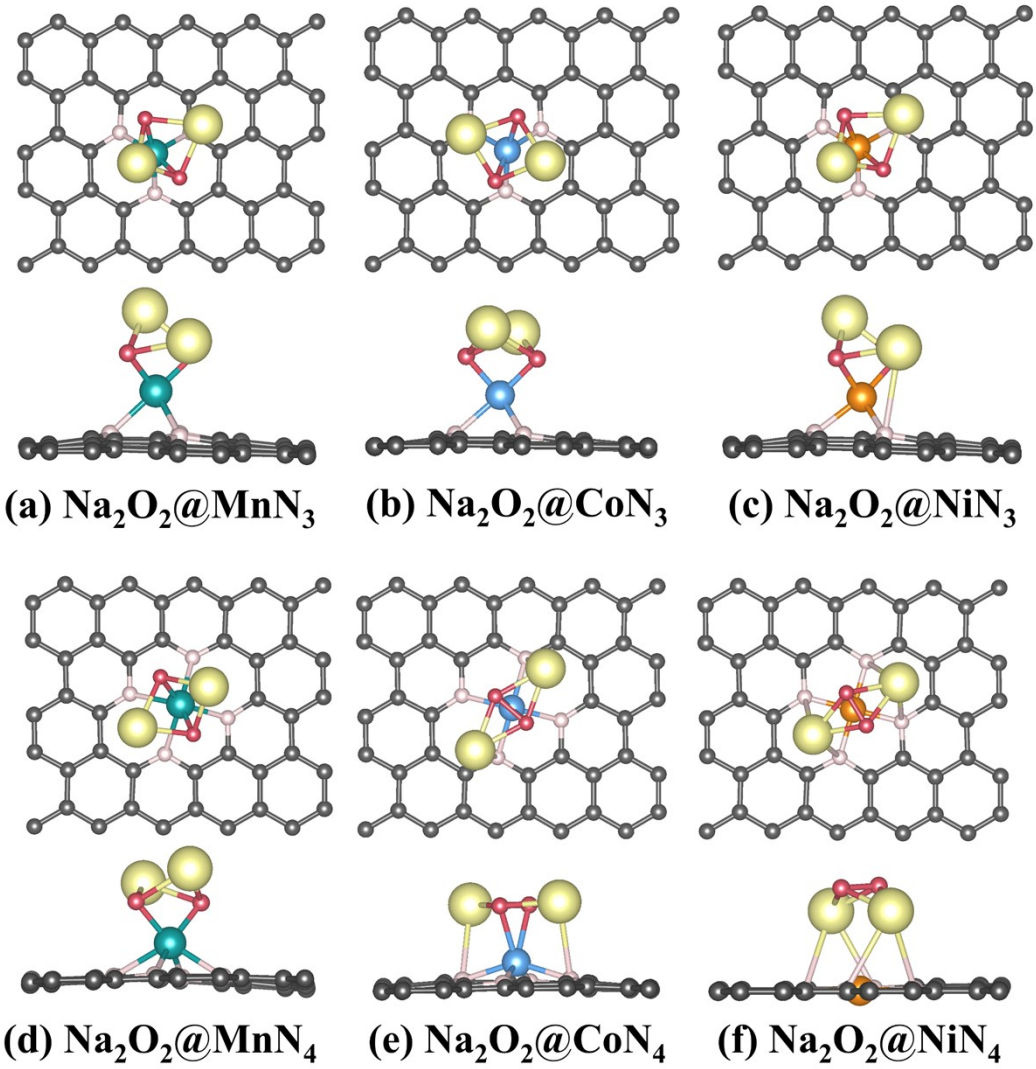

Figure S14. The optimized geometric structures of (a) Na_2O_2@MnN_3, (b) Na_2O_2@CoN_3, (c) Na_2O_2@NiN_3, (d) Na_2O_2@MnN_4, (e) Na_2O_2@CoN_4, and (f) Na_2O_2@NiN_4, respectively.

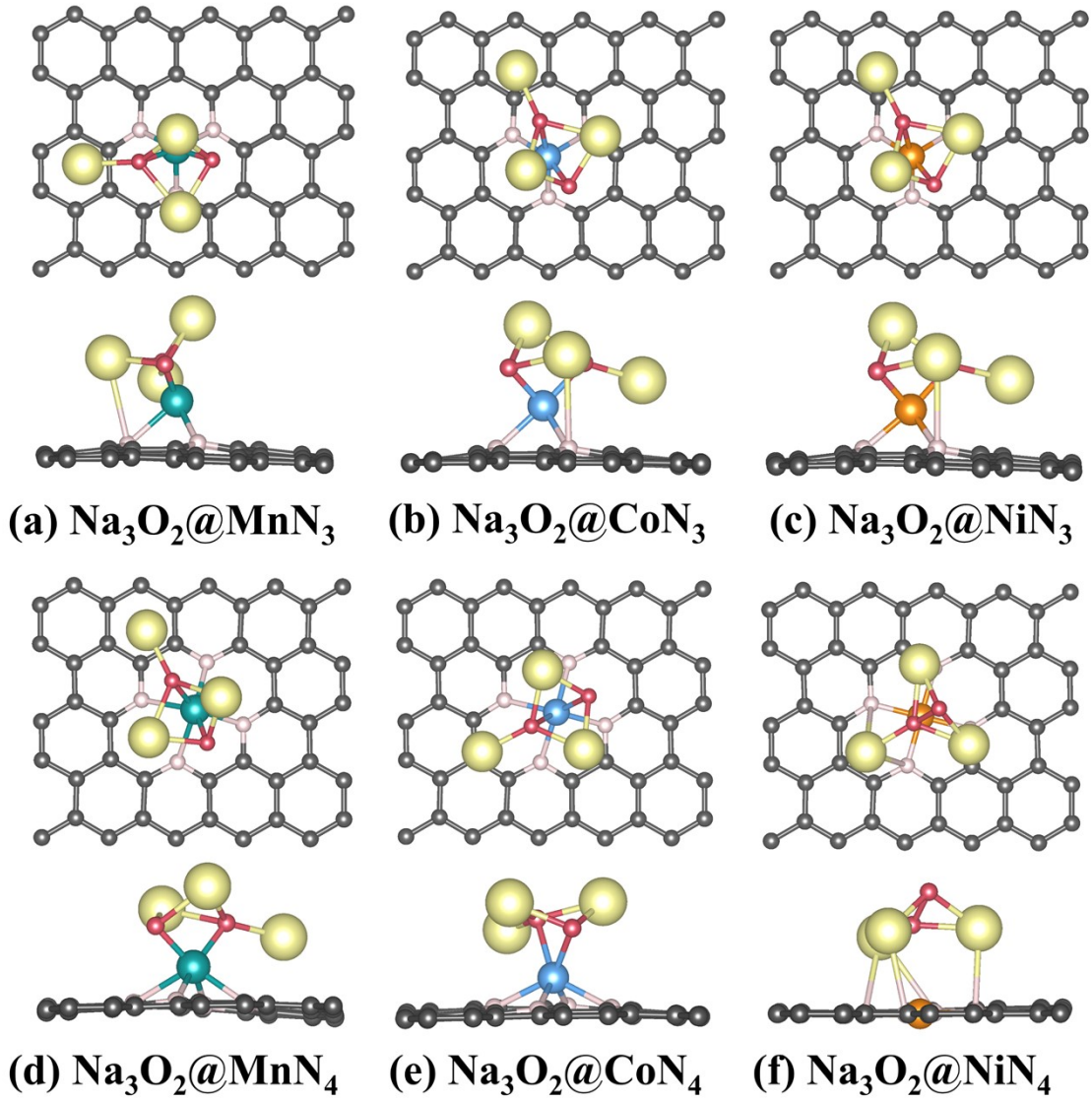

Figure S15. The optimized geometric structures of (a) $Na_3O_2@MnN_3$, (b) $Na_3O_2@CoN_3$, (c) $Na_3O_2@NiN_3$, (d) $Na_3O_2@MnN_4$, (e) $Na_3O_2@CoN_4$, and (f) $Na_3O_2@NiN_4$, respectively.

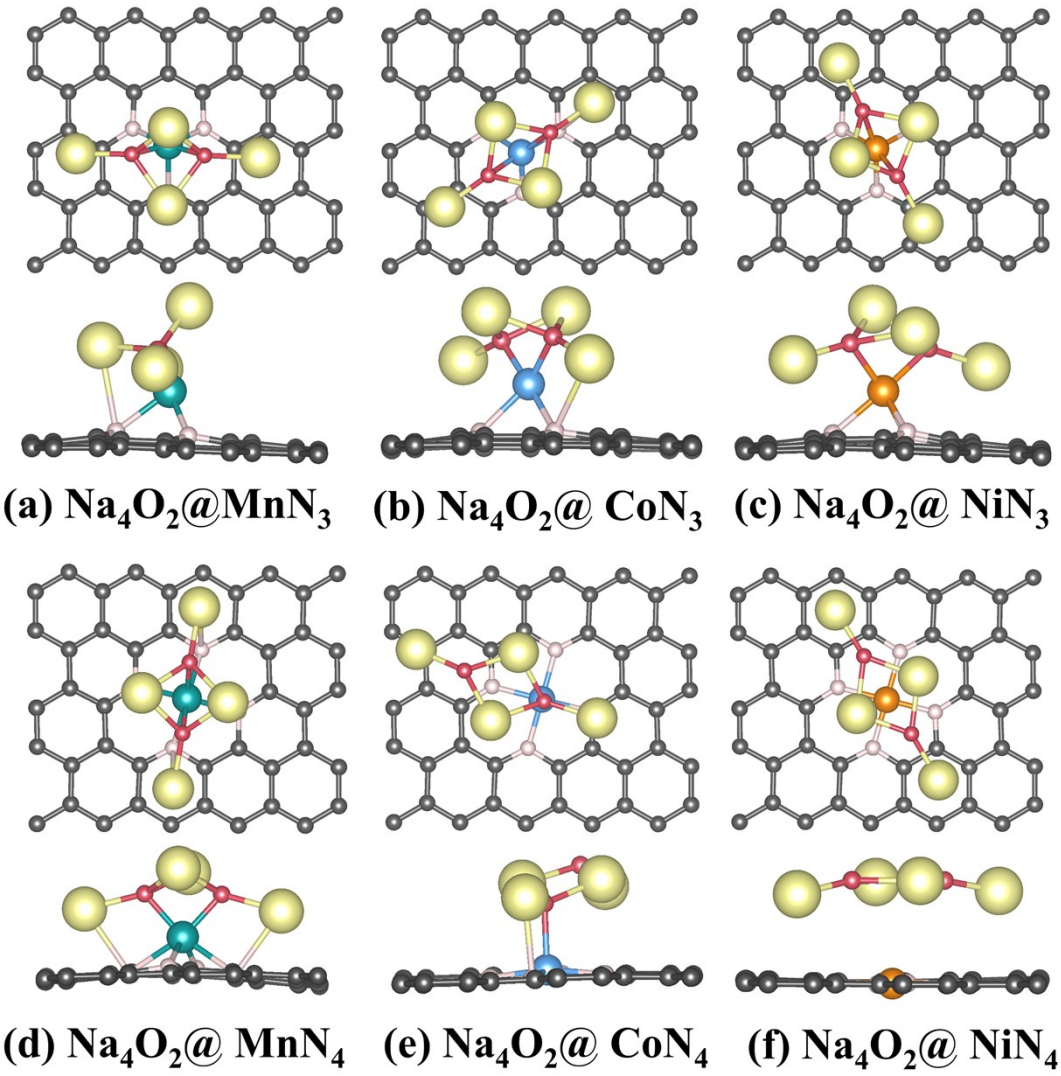

Figure S16. The optimized geometric structures of (a) Na_4O_2@MnN_3, (b) Na_4O_2@CoN_3, (c) Na_4O_2@NiN_3, (d) Na_4O_2@MnN_4, (e) Na_4O_2@CoN_4, and (f) Na_4O_2@NiN_4, respectively.

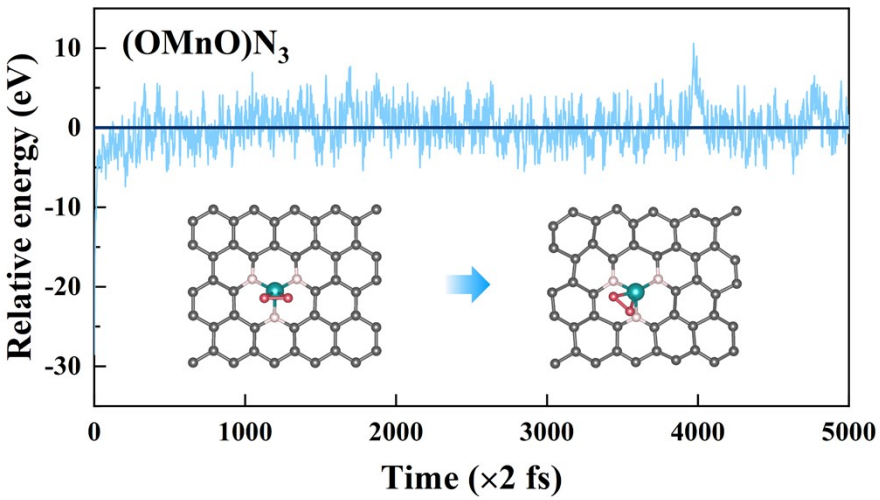

Figure S17. The variations of relative energy against the time for AIMD simulations of $(OMnO)N_3$ at 1200 K.

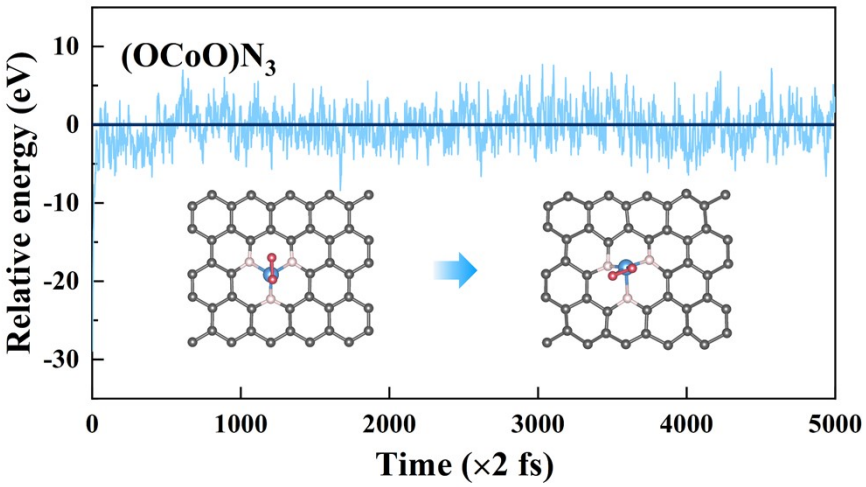

Figure S18. The variations of relative energy against the time for AIMD simulations of $(OCoO)N_3$ at 1200 K.

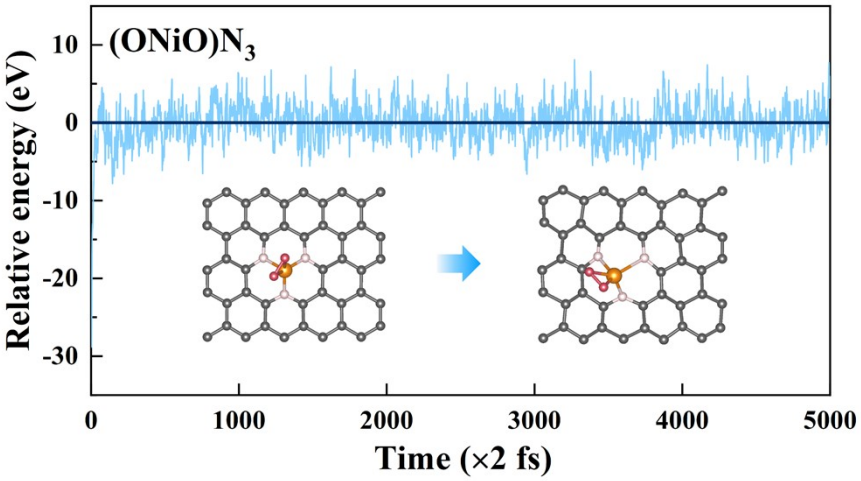

Figure S19. The variations of relative energy against the time for AIMD simulations of $(ONiO)N_3$ at 1200 K.

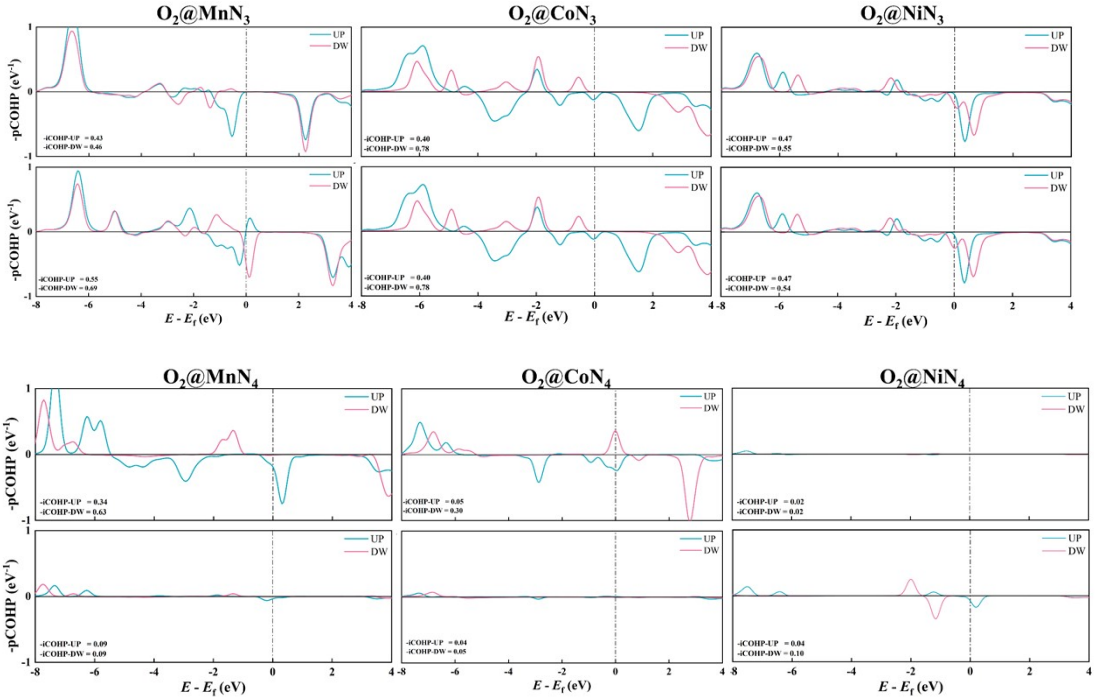

Figure S20. The projected Crystal Orbital Hamilton population (pCOHP) of O_2 adsorbed on the MnN_3, CoN_3, NiN_3, MnN_4, CoN_4, and NiN_4, respectively.

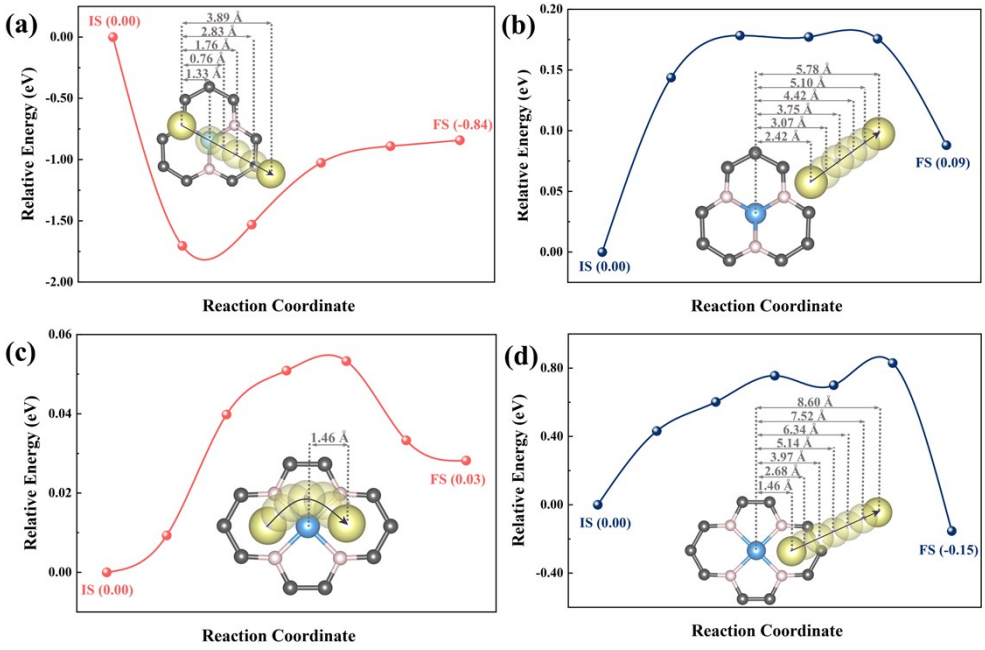

Figure S21. The relative energy profiles of (a) the proximal path and (b) the distal path of the Na atom on CoN_3, (c) the proximal path and (d) the distal path of the Na atom on CoN_4.

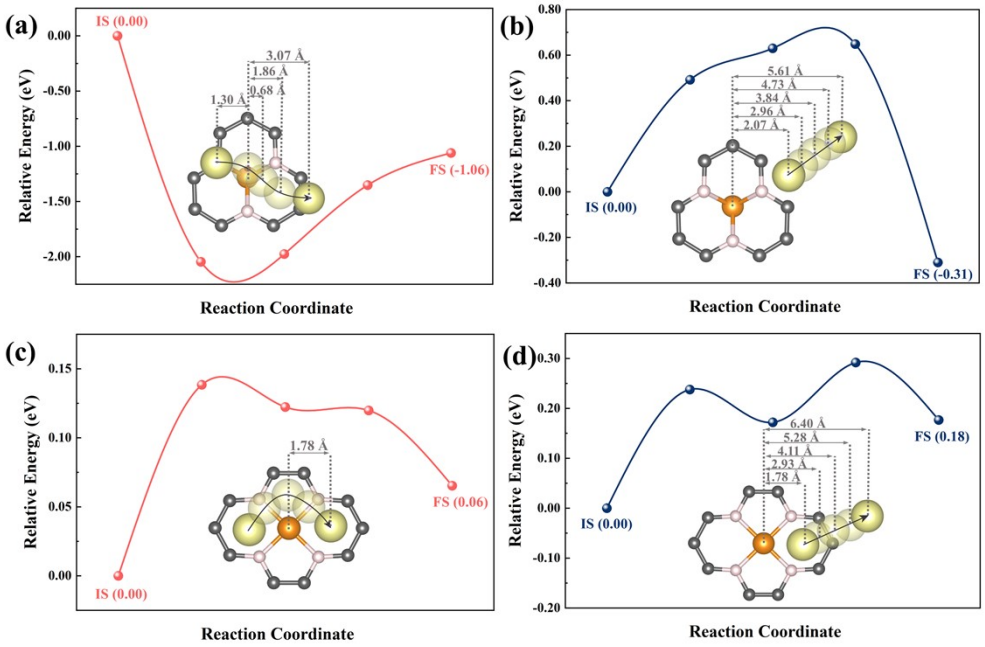

Figure S22. The relative energy profiles of (a) the proximal path and (b) the distal path of the Na atom on NiN_3, (c) the proximal path and (d) the distal path of the Na atom on NiN_4.

Table S1. The adsorption modes of oxygen on SACs with two coordination types.

Catalysts	The adsorption modes of oxygen
PtN_3	Side-on[11]
FeN_3	Side-on[12]
CoN_3	Side-on[3]
NiN_3	Side-on[14]
MnN_4	End-on[15]
CoN_4	End-on[12, 16-17]
NiN_4	End-on[16]

Table S2. The adsorption modes of metal atom or cluster on SACs with two coordination types.

Catalysts	The adsorbate	The adsorption modes
MoN_3	Li_2S_6	Top-on[18]
CoN_3	Co cluster	Top-on[19]
NiN_4-P-gr	Na	Hole-on[20]
NiN_4	Li	Hole-on[21]
PtN_4	Li	Hole-on[21]
CuN_4	Li	Hole-on[21]

References

1. Kresse, G.; Hafner, J. Ab Initiomolecular-Dynamics Simulation of the Liquid-Metal–Amorphous-Semiconductor Transition in Germanium. *Phys. Rev. B* **1994**, *49*, 14251-14269.

2. Perdew, J. P.Burke, K.; Ernzerhof, M. Generalized Gradient Approximation Made Simple. *Phys. Rev. Lett.* **1996**, *77*, 3865-3868.

3. Blöchl, P. E. Projector Augmented-Wave Method. *Phys. Rev. B* **1994**, *50*, 17953-17979.

4. Grimme, S. Semiempirical Gga-Type Density Functional Constructed with a Long-Range Dispersion Correction. *J. Comput. Chem.* **2006**, *27*, 1787-1799.

5. Li, J.-H.; Yu, Y.-X. Enhanced Catalytic Performance of Pillared δ-MnO_2 with Enlarged Layer Spaces for Lithium- and Sodium-Oxygen Batteries: A Theoretical Investigation. *Nanoscale* **2021**, *13*, 20637-20648.

6. Han, Y., et al. Experimental and Dft Studies of Oxygen Reduction Reaction Promoted by Binary Site Fe/Co–N–C Catalyst in Acid. *J. Electroanal. Chem.* **2022**, *914*.**7.** Ferrari, A. M.Pisani, C.Cinquini, F.Giordano, L.; Pacchioni, G. Cationic and Anionic Vacancies on the NiO(100) Surface: Dft+U and Hybrid Functional Density Functional Theory Calculations. *J. Chem. Phys.* **2007**, *127*.

8. Zuo, Z.Liu, S.Wang, Z.Liu, C.Huang, W.Huang, J.; Liu, P. Dry Reforming of Methane on Single-Site Ni/Mgo Catalysts: Importance of Site Confinement. *ACS Catal.* **2018**, *8*, 9821-9835.

9. Henkelman, G.; Jónsson, H. Improved Tangent Estimate in the Nudged Elastic Band

Method for Finding Minimum Energy Paths and Saddle Points. *J. Chem. Phys.* **2000**, *113*, 9978-9985.

10. Henkelman, G.Uberuaga, B. P.; Jónsson, H. A Climbing Image Nudged Elastic Band Method for Finding Saddle Points and Minimum Energy Paths. *J. Chem. Phys.* **2000**, *113*, 9901-9904.

11. Ji, W.; Meng, Y.; Fan, X.; Xiao, X.; Li, F., Theoretical insights into the oxidation of elemental mercury by O_2 on graphene-based Pt single-atom catalysts. *Chemosphere* **2022**, 297, 134178.

12. Li, Z.; Liu, F.; Chen, C.; Jiang, Y.; Ni, P.; Song, N.; Hu, Y.; Xi, S.; Liang, M.; Lu, Y., Regulating the N Coordination Environment of Co Single-Atom Nanozymes for Highly Efficient Oxidase Mimics. *Nano Lett.* **2023**, 23 (4), 1505-1513.

13. Li, Q. K.; Li, X. F.; Zhang, G.; Jiang, J., Cooperative Spin Transition of Monodispersed FeN_3 Sites within Graphene Induced by CO Adsorption. *J. Am. Chem. Soc. 2018*, 140 (45), 15149-15152.

14. Zang, W.; Sun, T.; Yang, T.; Xi, S.; Waqar, M.; Kou, Z.; Lyu, Z.; Feng, Y. P.; Wang, J.; Pennycook, S. J., Efficient Hydrogen Evolution of Oxidized Ni-N_3 Defective Sites for Alkaline Freshwater and Seawater Electrolysis. *Adv. Mater.* **2021**, 33 (8), 2003846.

15. Li, Y.; Ren, P.; Lu, X.; Zhang, J.; Yang, P.; Yang, X.; Wang, G.; Liu, A.; Wu, G.; An, M., Elucidating the role of P on Mn‐ and N‐doped graphene catalysts in promoting oxygen reduction: Density functional theory studies. *SusMat* **2023**, 3 (3), 390-401.

16. Fei, H.; Dong, J.; Feng, Y.; Allen, C. S.; Wan, C.; Volosskiy, B.; Li, M.; Zhao, Z.; Wang, Y.; Sun, H.; An, P.; Chen, W.; Guo, Z.; Lee, C.; Chen, D.; Shakir, I.; Liu, M.; Hu, T.; Li, Y.; Kirkland, A. I.; Duan, X.; Huang, Y., General synthesis and definitive structural identification of MN_4C_4 single-atom catalysts with tunable electrocatalytic activities. *Nat. Catal.* **2018**, 1 (1), 63-72.

17. Gao, J.; Yang, H. b.; Huang, X.; Hung, S.-F.; Cai, W.; Jia, C.; Miao, S.; Chen, H. M.; Yang, X.; Huang, Y.; Zhang, T.; Liu, B., Enabling Direct H_2O_2 Production in Acidic Media through Rational Design of Transition Metal Single Atom Catalyst. *Chem* **2020**, 6 (3), 658-674.

18. Yuan, C.; Song, X.; Zeng, P.; Liu, G.; Zhou, S.; Zhao, G.; Li, H.; Yan, T.; Mao, J.; Yang, H.; Cheng, T.; Wu, J.; Zhang, L., Precisely optimizing polysulfides adsorption and conversion by local coordination engineering for high-performance Li-S batteries. *Nano Energy* **2023**, 110.

19. Li, X.; Lu, G.; Wang, T.; Yang, J. Y.; Herrendorf, T.; Schwiderowski, P.; Schulwitz, J.; Chen, P.; Kleist, W.; Zhao, G.; Muhler, M.; Peng, B., Efficient Atomically Dispersed Co/N-C Catalysts for Formic Acid Dehydrogenation and Transfer Hydrodeoxygenation of Vanillin. *ChemSusChem* **2024**. e202300871

20. Qiu, D.; Zhao, W.; Zhang, B.; Ahsan, M. T.; Wang, Y.; Zhang, L.; Yang, X.; Hou, Y., Ni‐Single Atoms Modification Enabled Kinetics Enhanced and Ultra‐Stable Hard Carbon Anode for Sodium‐Ion Batteries. *Adv. Energy Mater.* **2024**, 14 (20), 2400002.

21. Zhai, P.; Wang, T.; Yang, W.; Cui, S.; Zhang, P.; Nie, A.; Zhang, Q.; Gong, Y.,

Uniform Lithium Deposition Assisted by Single‐Atom Doping toward High‐Performance Lithium Metal Anodes. *Adv. Energy Mater.* **2019**, 9 (18), 1804019.